

Article

# Low-Pt-Based Sn Alloy for the Dehydrogenation of Methylcyclohexane to Toluene: A Density Functional Theory Study

Kingsley Onyebuchi Obodo \*, Cecil Naphtaly Moro Ouma and Dmitri Bessarabov 

HySA-Infrastructure, Faculty of Engineering, North-West University, Private Bag X6001, Potchefstroom 2520, South Africa

\* Correspondence: ko.obodo@nwu.ac.za

**Abstract:** Spin-polarized van der Waals corrected density functional theory calculations were applied to Sn–Pt alloys with Pt content  $\leq 50\%$  (referred to as low Pt alloys) to evaluate their catalytic activity towards the dehydrogenation of methylcyclohexane (MCH), with the formation of toluene as product. The calculated adsorption energies of MCH, its intermediates and toluene showed that these molecules bind on the considered Sn–Pt alloys. Sn–Pt alloys had the lowest dehydrogenation energetics, indicating that the activity of this catalytic material is superior to that of a pristine Pt catalyst. Desorption of the intermediate species was feasible for all Sn–Pt alloy configurations considered. The catalytic dehydrogenation reaction energetics for the various Sn–Pt alloy configurations were more favourable than that achieved with pristine Pt surfaces. The current study should motivate experimental realization of Sn–Pt alloys for the catalytic dehydrogenation reaction of MCH.

**Keywords:** Sn–Pt surfaces; methylcyclohexane; toluene; dehydrogenation



**Citation:** Obodo, K.O.; Ouma, C.N.M.; Bessarabov, D. Low-Pt-Based Sn Alloy for the Dehydrogenation of Methylcyclohexane to Toluene: A Density Functional Theory Study. *Catalysts* **2022**, *12*, 1221. <https://doi.org/10.3390/catal12101221>

Academic Editors: Ning Rui and Lili Lin

Received: 12 September 2022

Accepted: 10 October 2022

Published: 12 October 2022

**Publisher's Note:** MDPI stays neutral with regard to jurisdictional claims in published maps and institutional affiliations.



**Copyright:** © 2022 by the authors. Licensee MDPI, Basel, Switzerland. This article is an open access article distributed under the terms and conditions of the Creative Commons Attribution (CC BY) license (<https://creativecommons.org/licenses/by/4.0/>).

## 1. Introduction

The development of green energy technology is attracting wide attention due to the need to replace health- and environment-damaging energy technologies. In this regard, the application of catalytic materials is rapidly expanding; hence, it is necessary to address energy challenges and cost implications for mass deployment. Several catalytic materials require the use of expensive noble metals for their catalytic reactions [1]. Various means of energy storage and deployment are available, all at various stages of development, deployment, and application.

The focus on energy storage and deployment via the use of liquid organic hydrogen carrier (LOHC) materials and, in particular, the development of more efficient and less costly catalytic materials for the dehydrogenation of a LOHC molecule are gaining significant traction [2–9]. LOHC molecules are organic compounds that consist of a carbon backbone, and, in some cases, various functional groups attached to it. LOHC molecules offer a very safe means for hydrogen storage and delivery because they are non-volatile organic liquids. LOHC molecules undergo reversible removal of hydrogen gas (dehydrogenation), resulting in a fully dehydrogenated aromatic compound that is hydrogen-lean, as well as the addition of hydrogen (hydrogenation), resulting in a fully hydrogenated aliphatic compound that is hydrogen-rich and hence, considered renewable [10–14].

The dehydrogenation reaction of the MCH to toluene molecule, for hydrogen storage and production, has been (and is being) extensively investigated [15–20]. The reaction of MCH to toluene is of interest, particularly because of the low cost of these molecules, high hydrogen storage density (6.2 wt%) and low toxicity of the dehydrogenated product, toluene [17,20].

Currently, Pt is the most widely used dehydrogenation catalyst for various LOHC molecules [4,20–30]. A reduction in the catalyst's Pt content, for the dehydrogenation

reaction, is essential in efforts to reduce costs associated with LOHCs as energy storage and transport materials. To this end, the use of Sn–Pt-based alloys in various catalytic reactions has been considered, and investigations initiated. The Sn–Pt-based alloys have been found to be useful as electrocatalysts in polymer electrolyte membrane fuel cells [31] and for the dehydrogenation of n-butane to n-butenes [32], selective hydrogenation of crotonaldehyde [33] and dehydrogenation of cyclohexene on Sn/Pt (111) surface alloys [34], and also for the hydrogenation of cyclohexanone on Pt–Sn surface alloys [35].

In this study, we consider application of van der Waals (vdW) spin-polarized density functional theory (DFT) calculations to different Sn–Pt alloys, where emphasis is on a low Pt content in the alloys. Specifically, we considered Sn–Pt alloys with Pt concentration  $\leq 50\%$ , i.e., SnPt, Sn<sub>2</sub>Pt, Sn<sub>3</sub>Pt<sub>2</sub> and Sn<sub>4</sub>Pt, for the catalytic dehydrogenation of MCH (C<sub>7</sub>H<sub>14</sub>) to toluene (C<sub>7</sub>H<sub>8</sub>). The considered Sn–Pt alloys were obtained using the convex hull procedure as implemented in the Materials Project (<https://materialsproject.org/>, accessed on 6 June 2021). For the various Sn–Pt alloy configurations considered, the most dominant surface, as evaluated using the Wulff construction, was taken as a representative surface for the catalytic reaction. The adsorption of the C<sub>7</sub>H<sub>14</sub> and dehydrogenation intermediates on the various surfaces of the Sn–Pt alloy configurations was considered. Stable surface–adsorbate complexes were observed for the various surface configurations. Overall, low Pt content of Sn–Pt alloys gave improved catalytic activity (better than with a pristine Pt catalyst) due to the lower dehydrogenation energy.

## 2. Results and Discussion

The results obtained for the catalytic properties of the various Sn–Pt alloy surfaces considered are now reported and discussed. First, the lowest energy absorption site for the C<sub>7</sub>H<sub>14</sub> molecule on the Sn–Pt alloy surfaces was evaluated, followed by the removal of each hydrogen molecule, as presented in Figure 1 and Table 1. This was carried out to obtain information on the dehydrogenation of the C<sub>7</sub>H<sub>14</sub> molecule (MCH) to the C<sub>7</sub>H<sub>8</sub> molecule (toluene).

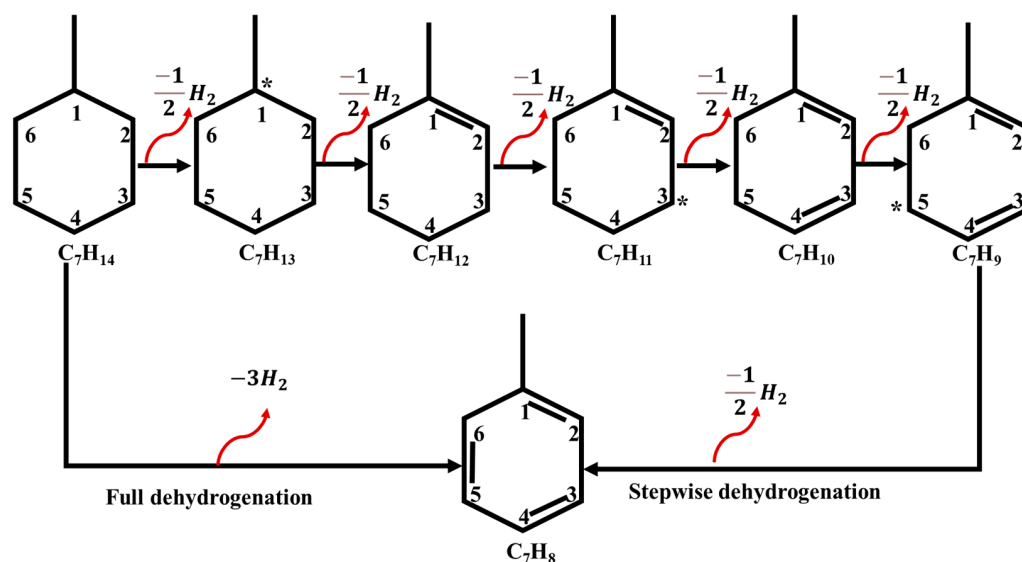


**Figure 1.** Full and stepwise dehydrogenation of methylcyclohexane to toluene molecule with the suggestive position of the single hydrogen atom ( $1/2 H_{2(g)}$ ) removal site in the molecules shown. The schematic shows that the  $1/2 H_{2(g)}$  removal proceeds in the order 1–6, which is an idealised configuration. The \* represents removal of one  $1/2 H_{2(g)}$  followed by the formation of a double C–C bond due to  $H_{2(g)}$  removal. The other pathways show the removal of  $3H_{2(g)}$ , resulting in the full dehydrogenation of methylcyclohexane to toluene.

**Table 1.** Methylcyclohexane (C<sub>7</sub>H<sub>14</sub>), the dehydrogenation intermediates and toluene (C<sub>7</sub>H<sub>8</sub>), and the calculated adsorption energies (in eV) for Sn–Pt surfaces considered.

Molecules	Sn <sub>4</sub> Pt	Sn <sub>2</sub> Pt	Sn <sub>3</sub> Pt <sub>2</sub>	SnPt
C <sub>7</sub> H <sub>14</sub>	−0.87	−0.91	−0.73	−2.97
C <sub>7</sub> H <sub>13</sub>	−3.76	−2.11	−3.51	−3.52
C <sub>7</sub> H <sub>12</sub>	−2.79	−1.31	−2.31	−3.05
C <sub>7</sub> H <sub>11</sub>	−3.68	−2.07	−3.32	−4.57
C <sub>7</sub> H <sub>10</sub>	−3.77	−1.32	−2.34	−3.91
C <sub>7</sub> H <sub>9</sub>	−4.24	−1.91	−3.11	−4.52
C <sub>7</sub> H <sub>8</sub>	−3.55	−1.03	−0.75	−3.29

Different approximations play a role in the calculated energetics of a material. The full dehydrogenation of the dominant Pt surface, the Pt (111) surface, was determined using the same approximations as presented in Section 2 to benchmark the various Sn–Pt alloys considered. The calculated dehydrogenation energy of the reaction from C<sub>7</sub>H<sub>14</sub> to C<sub>7</sub>H<sub>8</sub> on the Pt (111) surface was 89.28 kJ/mol. This is higher than recorded in previous theoretical studies [18] and an experimental value of 68.3 kJ/mol; it is attributed to the DFT approximations used in the calculations [16,36]. The application of DFT calculations is known to predict and describe various properties of different materials [1,30,37,38]. As such, our findings here show that a reduction in Pt concentration and alloying with Sn results in overall qualitative and quantitative improvement of the catalytic properties towards the dehydrogenation reaction of C<sub>7</sub>H<sub>14</sub> to C<sub>7</sub>H<sub>8</sub>.

### 2.1. Adsorption Energies of C<sub>7</sub>H<sub>14</sub>(g) and Its Intermediates on the Surfaces of Sn–Pt Alloys

The adsorption energies of C<sub>7</sub>H<sub>14</sub> and its intermediate products, as well as C<sub>7</sub>H<sub>8</sub>, obtained because of 1/2H<sub>2(g)</sub> removal on the Sn–Pt surfaces, were evaluated using Equation (2), see Section 3. We wished to determine whether these molecules can stably adsorb on the Sn–Pt surfaces considered and effectively partake in the dehydrogenation reaction. The adsorption locator module in BIOVIA Materials Studio was used to determine the optimal adsorption configurations for the C<sub>7</sub>H<sub>14</sub> molecule, as described in Section 3.

The calculated adsorption energies for the C<sub>7</sub>H<sub>14</sub> molecule and its intermediate products, as well as the C<sub>7</sub>H<sub>8</sub> molecule, were negative on the Sn<sub>4</sub>Pt, Sn<sub>2</sub>Pt, Sn<sub>3</sub>Pt<sub>2</sub> and SnPt alloy surfaces considered—as also determined in our previous studies [17]. The implication is that C<sub>7</sub>H<sub>14</sub> and its intermediates products, as well as C<sub>7</sub>H<sub>8</sub>, would favourably be formed on the considered surfaces and C<sub>7</sub>H<sub>14</sub> would be dehydrogenated to form C<sub>7</sub>H<sub>8</sub>. Furthermore, the adsorption of C<sub>7</sub>H<sub>14</sub> on the Sn–Pt alloy surface had the lowest adsorption energy, compared to other intermediates and the C<sub>7</sub>H<sub>8</sub>. The most strongly adsorbed molecules were C<sub>7</sub>H<sub>9</sub>, C<sub>7</sub>H<sub>11</sub>, C<sub>7</sub>H<sub>13</sub> and C<sub>7</sub>H<sub>11</sub> for the Sn<sub>4</sub>Pt, Sn<sub>2</sub>Pt, Sn<sub>3</sub>Pt<sub>2</sub> and SnPt alloy surfaces, respectively. According to results presented in Table 1, there was no clear trend for the adsorption C<sub>7</sub>H<sub>14</sub>, its intermediates and the C<sub>7</sub>H<sub>8</sub> molecule.

### 2.2. Pathways and Energetics of the Dehydrogenation Reaction

#### 2.2.1. Monoatomic Removal of Hydrogen (1/2H<sub>2(g)</sub>)

The dehydrogenation reaction of C<sub>7</sub>H<sub>14</sub> to the C<sub>7</sub>H<sub>8</sub> molecule on the Sn–Pt-based alloy surfaces was undertaken via the removal of a single hydrogen atom from the C<sub>7</sub>H<sub>14</sub> until C<sub>7</sub>H<sub>8</sub> was obtained. To carry out the removal of a single hydrogen atom, a choice should be made on the order of removing the 1/2H<sub>2(g)</sub>. The procedure used in previous studies, which entails removal of a single hydrogen atom, was applied [12,18,28,39,40]. For the Sn–Pt-based alloy surfaces, the 1/2H<sub>2(g)</sub> removal energies were obtained using Equation (1) for the removal, where E<sub>RxN</sub> is

$$E_{\text{RxN}} = (E_{\text{Surf+Mol-H}} + E_{\text{Surf+H}}) - (E_{\text{Surf+Mol}} + E_{\text{Surf}}) \quad (1)$$

Here,  $E_{R_{XN}}$ ,  $E_{Surf+Mol-H}$ ,  $E_{Surf+H}$ ,  $E_{Surf+Mol}$ , and  $E_{Surf}$  are the reaction energies for H removal, the total energy of the surface with the molecules and removed hydrogen, the total energy of the surface with hydrogen, the total energy of the surface with the molecule without removed hydrogen, and the total energy of the surface alone. The surface here refers to the Sn–Pt-based alloy surfaces considered.

As an illustration, the first  $1/2H_{2(g)}$  removal from the MCH molecule was considered. The  $1/2H_{2(g)}$  removal energy was obtained using  $E_{R_{XN}} = (E_{Surf+C_7H_{13}} + E_{Surf+H}) - (E_{Surf+C_7H_{14}} + E_{Surf})$ , where  $E_{Surf+C_7H_{14}}$ ,  $E_{Surf+C_7H_{13}}$ ,  $E_{Surf}$  and  $E_{Surf+H}$  are the calculated total energies of the surface– $C_7H_{14}$  system, surface– $C_7H_{13}$  (MCH with a removed  $1/2H_{2(g)}$  atom) system, surface alone, and a dissociated H adsorbed on the surface, respectively. The calculated removal energies for the single hydrogen atom  $C_7H_{14}$ , leading to the different intermediates and formation of  $C_7H_8$ , are tabulated in Table 2 for the Sn–Pt-based alloy surfaces considered.

**Table 2.** Calculated energy for the removal of a half hydrogen molecule ( $1/2H_{2(g)}$ ) up to the sixth hydrogen atom ( $3H_{2(g)}$ ) on the different surfaces considered for the Sn–Pt alloys.

Sn–Pt Alloys	Surface	1H	2H	3H	4H	5H	6H
Sn <sub>3</sub> Pt <sub>2</sub>	(0 0 2)	−69.76	62.05	67.81	58.59	45.83	104.48
Sn <sub>4</sub> Pt	(1 0 1)	−78.49	39.11	79.04	−43.45	74.82	−56.41
Sn <sub>2</sub> Pt	(1 1 1)	81.83	23.36	91.52	36.13	63.78	−38.08
SnPt	(1 −1 0)	143.75	−8.03	18.08	29.03	60.80	3.97

Figure 1 shows a schematic of the C atoms that form the benzene ring of  $C_7H_{14(g)}$ . The procedure was followed for the removal of half hydrogen molecule ( $1/2H_{2(g)}$ ) up to the sixth hydrogen atom ( $3H_{2(g)}$ ) on the different surfaces considered for the Sn–Pt-based alloys. This is an elaborate process, as described above. The calculated energy for the removal of each  $1/2H_{2(g)}$  on the Sn–Pt-based alloy surfaces is presented in Table 3. It is observed that the highest removal energy of H atom on the Sn–Pt-based alloy surfaces does not follow any specific trend for the different surfaces and alloys considered.

**Table 3.** Calculated reaction energies on the Sn–Pt-based alloy surfaces (in eV) for the pathways A–D.

Pathways		A			B		C		D
Sn–Pt Alloys	Surfaces	H <sub>2</sub>	H <sub>2</sub>	H <sub>2</sub>	H <sub>2</sub>	2H <sub>2</sub>	2H <sub>2</sub>	H <sub>2</sub>	3H <sub>2</sub>
Sn <sub>3</sub> Pt <sub>2</sub>	(0 0 2)	−7.71	126.41	150.31	−7.71	276.72	118.70	150.31	83.33
Sn <sub>4</sub> Pt	(1 0 1)	−39.39	35.59	18.41	−39.39	54.00	−3.80	18.41	4.41
Sn <sub>2</sub> Pt	(1 1 1)	105.19	127.65	25.70	105.19	153.36	232.84	25.70	85.72
SnPt	(1 −1 0)	135.72	47.11	64.77	135.72	111.88	182.83	64.77	79.45
Pt	(1 1 1)								89.28

The  $1/2H_{2(g)}$  removal pathways from the  $C_7H_{14}$  molecule on the SnPt, Sn<sub>2</sub>Pt, Sn<sub>3</sub>Pt<sub>2</sub> and Sn<sub>4</sub>Pt surfaces were 541263, 543216, 546123, and 432165, respectively (numbers refer to positions of the aromatic ring: see Figure 1). For the different alloy surfaces, the pathways were not the same. The removal of a single hydrogen atom from the different alloys followed different pathways. However, we did observe that the next nearest  $1/2H_{2(g)}$  to the first abstracted  $1/2H_{2(g)}$  was always preferred, irrespective of the Sn–Pt-based alloy surface. This is a result of the ease of formation of a double bond due to the formation of a free radical initially. The above observation would subsequently reduce the number of calculations required to be carried out in future investigations.

### 2.2.2. Possible Pathways for $H_{2(g)}$ Removal

The different possible pathways for  $H_{2(g)}$  abstraction resulting in the dehydrogenation reaction of  $C_7H_{14}$  to the  $C_7H_8$  molecule on the Sn–Pt-based alloy surfaces are presented in

Table 3. This has been shown in previous studies [12,18]. The reaction proceeds stepwise via four different pathways, as presented in Table 3. These pathways entail: (i) the removal of each  $H_{2(g)}$ , as presented in step A; (ii) the removal of  $H_{2(g)}$  followed by  $2H_{2(g)}$ , as presented in step B; (iii) the removal of  $2H_{2(g)}$  followed by  $H_{2(g)}$ , as presented in step C; and (iv) the removal of all  $3H_{2(g)}$  in a single step. The removal of all  $3H_{2(g)}$  is the full dehydrogenation reaction of MCH to toluene, as presented in pathway D. The calculated reaction energies for these pathways and each step were obtained using a modified version of Equation (1).

Taking pathways A, B and C into consideration, the highest energy step for the removal of the first  $H_{2(g)}$  on the different Sn–Pt-based alloy surfaces does not follow the similar or equivalent steps or a specific trend. The difference in pathways is attributed to the nature of each of the Sn–Pt-based alloy surfaces considered here and their electronic properties. Thus, different steps are the reaction-limiting cases for the pathways A, B and C. However, no specific trend in terms of reaction pathway was observed. The implication is that Sn–Pt-based catalysts do not follow any specific trend in terms of the dehydrogenation pathways. For the removal of  $3H_2$ , which results in the overall dehydrogenation of  $C_7H_{14}$  to  $C_7H_8$ , which is pathway D, the pristine Pt has the highest dehydrogenation energy (compared to the various alloys considered). The implication is that alloying Pt with Sn leads to a reduction in the overall activation energy and hence an improvement in the catalytic properties of the material.

The Brønsted–Evans–Polanyi linear scaling relationship uses both the reaction energies and activation energies of the dehydrogenation reactions to determine the activation energy, as reported earlier [41], as has been applied to some studies [15,42,43]. The surface with the highest reaction energy also has the highest activation energy, as determined in an earlier investigation by Obodo et al. [15]. Thus, the catalytic activation energy can be described using only the reaction energies.

### 3. Computational Method

The spin-polarized vdW DFT [44–46] calculations were carried as implemented in the CASTEP code [47,48] within the Materials Studio package. The Perdew–Burke–Ernzerhof form [49] of the generalized gradient approximation [50,51] exchange–correlation functional and ultra-soft pseudopotential were applied to describe the electron–ion interactions. The Tkatchenko–Scheffler method [52] for semi-empirical dispersion correction was applied to account for the vdW interactions.

The SnPt,  $Sn_2Pt$ ,  $Sn_3Pt_2$  and  $Sn_4Pt$  in the P63/MMC, P63/MMC, P63/MMC and CCCA space groups were considered. These configurations were obtained using the convex hull from the Materials Project database as the most optimal structures. The various surface configurations for the Sn–Pt-based alloys were determined. We found that the (1 –1 0), (1 1 1), (0 0 2) and (1 –1 0) were the most dominant surface configurations, using the Wulff construction as implemented in the morphology module of the Materials Studio 2020 suite for the SnPt,  $Sn_2Pt$ ,  $Sn_3Pt_2$  and  $Sn_4Pt$ , respectively, as presented in Figure 2. These configurations were used to create surface slabs with 4/5 atomic layers in the c-axis. The  $k$ -point mesh separation of  $0.07 \text{ \AA}^{-1}$ , an adequately converged kinetic energy cut-off of 408.20 eV, and  $10^{-6}$  eV/atom convergence criteria for the calculated total energies were applied to optimize the various alloys of the Sn–Pt unit cell considered. The forces in the various alloys of the Sn–Pt unit cell considered were converged up to  $0.03 \text{ eV/\AA}$  for the full geometric optimization.

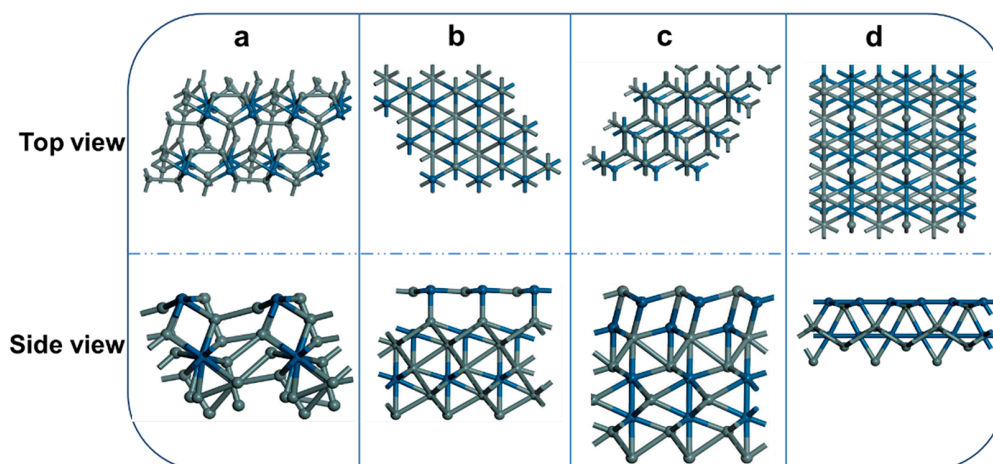


**Figure 2.** Schematic ball and stick model of the Sn–Pt alloy surfaces showing the top and side view, where (a) Sn<sub>4</sub>Pt, (b) Sn<sub>3</sub>Pt<sub>2</sub>, (c) Sn<sub>2</sub>Pt, and (d) SnPt. The blue and grey balls are the Pt and Sn atoms, respectively.

Various super-cell slabs of the Sn–Pt alloys with vacuum distance 15 Å, and consisting of five-layer slabs, were used for all of the calculations in this study. The vacuum distance applied in the z-direction was adequate to prevent periodic image interactions [53]. The convergence criteria enforced for the unit cell and the super-cell slab calculations were the same. For the super-cell slab calculations, the volume was fixed with the atomic positions optimized. The size of the molecular adsorbates considered, and tractability of the calculations, influenced the choice for the area of the surface slab (length × width). To avoid, first, the straining of the relaxed molecular adsorbates on the surface and, second, the interaction of mirror images, >5 Å was added to the length and width of the longest molecular species to form the length and width of the surface slab, as consistent with previous studies [12].

The lowest energy adsorption sites for the molecular adsorbates (C<sub>7</sub>H<sub>14</sub>, C<sub>7</sub>H<sub>13</sub>, C<sub>7</sub>H<sub>12</sub>, C<sub>7</sub>H<sub>11</sub>, C<sub>7</sub>H<sub>10</sub>, C<sub>7</sub>H<sub>9</sub> and C<sub>7</sub>H<sub>8</sub>) on the Sn–Pt alloy surfaces were evaluated using the adsorption locator module. The latter has been applied in various studies to evaluate the lowest energy surface–adsorbate configuration (SAC) [4,12,18]. The molecular adsorbates were pre-adsorbed to determine the optimal SAC, which is the lowest energy configuration. The determined optimal surface–adsorbate configurations were subsequently relaxed using vdW corrected spin-polarized DFT calculations to determine the final configurations and total energies [54]. Next, the adsorption energy ( $E_{\text{Ads}}$ ) of each SAC on the Sn–Pt surfaces was evaluated using Equation (2) [18,55]

$$E_{\text{Ads}} = E_{\text{SAC}} - E_{\text{Surf}} - E_{\text{mol}} \quad (2)$$

where  $E_{\text{SAC}}$ ,  $E_{\text{Surf}}$ , and  $E_{\text{mol}}$  are the following, respectively: the total energy of the Sn–Pt surface slabs with the C<sub>7</sub>H<sub>14</sub> molecule and its intermediates, the total energy of the Sn–Pt surface slabs without the C<sub>7</sub>H<sub>14</sub> molecule and its intermediates, and the total energy of the C<sub>7</sub>H<sub>14</sub> molecule and its intermediates. The activation energies were not considered in the current investigation (as in our previous studies) [15].

#### 4. Conclusions

DFT with spin-polarized vdW correction was applied to investigate Sn–Pt-based alloy surfaces, specifically, low-concentration Sn–Pt-based alloy surfaces. The convex hull and Wulff construction were used to determine the dominant surfaces. The calculated adsorption energies of C<sub>7</sub>H<sub>14</sub>, its intermediates and C<sub>7</sub>H<sub>8</sub> were determined—they absorb exothermically on the considered Sn–Pt-based alloy surfaces.

The determined reaction energies for the various surfaces of Sn–Pt-based alloys demonstrated that the dehydrogenation pathways differ. The Sn<sub>4</sub>Pt (101) surface had the lowest overall dehydrogenation energy of all the considered surfaces. Hence, among the Sn–Pt-based alloys, the Sn<sub>4</sub>Pt alloy is the best dehydrogenation catalyst. Furthermore, all the considered Sn–Pt-based alloys considered in this study had lower dehydrogenation energies compared to Pt (Pt being the optimal dehydrogenation catalyst to date).

**Author Contributions:** Conceptualization, K.O.O.; Methodology, K.O.O.; Writing—original draft, K.O.O.; Writing—review and editing, K.O.O., C.N.M.O. and D.B.; Funding acquisition, D.B. All authors have read and agreed to the published version of the manuscript.

**Funding:** This project has received funding from the Fuel Cells and Hydrogen 2 Joint Undertaking under grant agreement No 101007223. This Joint Undertaking receives support from the European Union’s Horizon 2020 Research and Innovation programme, Hydrogen Europe, and Hydrogen Europe research. The project also received funding from DSI South Africa and HySA Infrastructure Centre of Competence, Faculty of Engineering, North-West University via KP5 grant.

**Data Availability Statement:** Data used in the study are included in the manuscript.

**Acknowledgments:** The authors thank the Centre for High Performance Computing (CHPC), Cape Town, South Africa for computational resources used in this study and the HySA-Infrastructure Centre of Competence, Faculty of Engineering, North-West University for financial support. KOO thanks National Institute of Theoretical and Computational Sciences, Johannesburg, South Africa.

**Conflicts of Interest:** The authors declare no conflict of interest.

## References

1. Obodo, K.O.; Ouma, C.N.M.; Bessarabov, D. Low-Temperature Water Electrolysis. In *Power to Fuel: How to Speed Up a Hydrogen Economy*; Spazzafumo, G., Ed.; Elsevier: Amsterdam, The Netherlands, 2021; pp. 1–287.
2. Bessarabov, D.; Human, G.; Kruger, A.J.; Chiuta, S.; Modisha, P.M.; du Preez, S.P.; Oelofse, S.P.; Vincent, I.; Van Der Merwe, J.; Langmi, H.W.; et al. South African Hydrogen Infrastructure (HySA Infrastructure) for Fuel Cells and Energy Storage: Overview of a Projects Portfolio. *Int. J. Hydrogen Energy* **2017**, *42*, 13568–13588. [[CrossRef](#)]
3. Wulf, C.; Zapp, P. Assessment of System Variations for Hydrogen Transport by Liquid Organic Hydrogen Carriers. *Int. J. Hydrogen Energy* **2018**, *43*, 11884–11895. [[CrossRef](#)]
4. Modisha, P.M.; Ouma, C.N.M.; Garidzirai, R.; Wasserscheid, P.; Bessarabov, D. The Prospect of Hydrogen Storage Using Liquid Organic Hydrogen Carriers. *Energy Fuels* **2019**, *33*, 2778–2796. [[CrossRef](#)]
5. Jo, Y.; Oh, J.; Kim, D.; Park, J.H.; Baik, H.; Suh, Y.-W. Recent Progress in Dehydrogenation Catalysts for Heterocyclic and Homocyclic Liquid Organic Hydrogen Carriers. *Korean J. Chem. Eng.* **2022**, *39*, 20–37. [[CrossRef](#)]
6. Ye, H.-L.; Liu, S.-X.; Zhang, C.; Cai, Y.-Q.; Shi, Y.-F. Dehydrogenation of Methylcyclohexane over Pt-Based Catalysts Supported on Functional Granular Activated Carbon. *RSC Adv.* **2021**, *11*, 29287. [[CrossRef](#)]
7. Wijayanta, A.T.; Oda, T.; Purnomo, C.W.; Kashiwagi, T.; Aziz, M. Liquid Hydrogen, Methylcyclohexane, and Ammonia as Potential Hydrogen Storage: Comparison Review. *Int. J. Hydrogen Energy* **2019**, *44*, 15026–15044. [[CrossRef](#)]
8. Niermann, M.; Timmerberg, S.; Drünert, S.; Kaltschmitt, M. Liquid Organic Hydrogen Carriers and Alternatives for International Transport of Renewable Hydrogen. *Renew. Sustain. Energy Rev.* **2021**, *135*, 110171. [[CrossRef](#)]
9. Kwak, Y.; Kirk, J.; Moon, S.; Ohm, T.; Lee, Y.J.; Jang, M.; Park, L.H.; Ahn, C.; Jeong, H.; Sohn, H.; et al. Hydrogen Production from Homocyclic Liquid Organic Hydrogen Carriers (LOHCs): Benchmarking Studies and Energy-Economic Analyses. *Energy Convers. Manag.* **2021**, *239*, 114124. [[CrossRef](#)]
10. Do, G.; Preuster, P.; Aslam, R.; Bösmann, A.; Müller, K.; Arlt, W.; Wasserscheid, P. Hydrogenation of the Liquid Organic Hydrogen Carrier Compound Dibenzyltoluene—Reaction Pathway Determination by <sup>1</sup>H NMR Spectroscopy. *React. Chem. Eng.* **2016**, *1*, 313–320. [[CrossRef](#)]
11. Leinweber, A.; Müller, K. Hydrogenation of the LOHC Compound Monobenzyl Toluene—Reaction Pathway and Kinetic Effects. *Energy Technol.* **2017**, *6*, 513–520. [[CrossRef](#)]
12. Ouma, C.N.M.; Modisha, P.; Bessarabov, D. Insight into the Adsorption of a Liquid Organic Hydrogen Carrier, Perhydro-*i*-Dibenzyltoluene (*i* = *m*, *o*, *p*), on Pt, Pd and PtPd Planar Surfaces. *RSC Adv.* **2018**, *8*, 31895–31904. [[CrossRef](#)]
13. Singh, E.; Kim, K.S.; Yeom, G.Y.; Nalwa, H.S. Two-Dimensional Transition Metal Dichalcogenide-Based Counter Electrodes for Dye-Sensitized Solar Cells. *RSC Adv.* **2017**, *7*, 28234–28290. [[CrossRef](#)]
14. Ouma, C.N.M.; Obodo, K.O.; Modisha, P.M.; Rhyman, L.; Ramasami, P.; Bessarabov, D. Effect of Chalcogen (S, Se and Te) Surface Additives on the Dehydrogenation of a Liquid Organic Hydrogen Carrier System, Octahydroindole–Indole, on a Pt (1 1 1) Surface. *Appl. Surf. Sci.* **2021**, *566*, 150636. [[CrossRef](#)]

15. Obodo, K.O.; Ouma, C.N.M.; Bessarabov, D. Modified Pt (2 1 1) and (3 1 1) Surfaces towards the Dehydrogenation of Methylcyclohexane to Toluene: A Density Functional Theory Study. *Appl. Surf. Sci.* **2022**, *584*, 152590. [CrossRef]
16. Chen, F.; Huang, Y.; Mi, C.; Wu, K.; Wang, W.; Li, W.; Yang, Y. Density Functional Theory Study on Catalytic Dehydrogenation of Methylcyclohexane on Pt(111). *Int. J. Hydrogen Energy* **2020**, *45*, 6727–6737. [CrossRef]
17. Alhumaidan, F.; Cresswell, D.; Garforth, A. Hydrogen Storage in Liquid Organic Hydride: Producing Hydrogen Catalytically from Methylcyclohexane. *Energy Fuels* **2011**, *25*, 4217–4234. [CrossRef]
18. Obodo, K.O.; Ouma, C.N.M.; Modisha, P.M.; Bessarabov, D. Density Functional Theory Calculation of Ti<sub>3</sub>C<sub>2</sub> MXene Monolayer as Catalytic Support for Platinum towards the Dehydrogenation of Methylcyclohexane. *Appl. Surf. Sci.* **2020**, *529*, 147186. [CrossRef]
19. Yolcular, S.; Olgun, Ö. Hydrogen Storage in the Form of Methylcyclohexane. *Energy Sources Part A Recover. Util. Environ. Eff.* **2007**, *30*, 149–256. [CrossRef]
20. Boufaden, N.; Akkari, R.; Pawelec, B.; Fierro, J.L.G.; Zina, M.S.; Ghorbel, A. Dehydrogenation of Methylcyclohexane to Toluene over Partially Reduced Silica-Supported Pt-Mo Catalysts. *J. Mol. Catal. A Chem.* **2016**, *420*, 96–106. [CrossRef]
21. Sun, G.; Zhao, Z.J.; Mu, R.; Zha, S.; Li, L.; Chen, S.; Zang, K.; Luo, J.; Li, Z.; Purdy, S.C.; et al. Breaking the Scaling Relationship via Thermally Stable Pt/Cu Single Atom Alloys for Catalytic Dehydrogenation. *Nat. Commun.* **2018**, *9*, 4454. [CrossRef]
22. Maatman, R.W.; Mahaffy, P.; Hoekstra, P.; Addink, C. The Preparation of Pt-Alumina Catalyst and Its Role in Cyclohexane Dehydrogenation. *J. Catal.* **1971**, *23*, 105–118. [CrossRef]
23. Sugiura, Y.; Nagatsuka, T.; Kubo, K.; Hirano, Y.; Nakamura, A.; Miyazawa, K.; Iizuka, Y.; Furuta, S.; Iki, H.; Higo, T.; et al. Dehydrogenation of Methylcyclohexane over Pt/TiO<sub>2</sub>-Al<sub>2</sub>O<sub>3</sub> Catalysts. *Chem. Lett.* **2017**, *46*, 1601–1604. [CrossRef]
24. Lup, A.N.K.; Abnisa, F.; Daud, W.M.A.W.; Aroua, M.K. A Review on Reactivity and Stability of Heterogeneous Metal Catalysts for Deoxygenation of Bio-Oil Model Compounds. *J. Ind. Eng. Chem.* **2017**, *56*, 1–34. [CrossRef]
25. Antolini, E. Pt-Ni and Pt-M-Ni (M = Ru, Sn) Anode Catalysts for Low-Temperature Acidic Direct Alcohol Fuel Cells: A Review. *Energies* **2017**, *10*, 42. [CrossRef]
26. Frontera, P.; Macario, A.; Ferraro, M.; Antonucci, P. Supported Catalysts for CO<sub>2</sub> Methanation: A Review. *Catalysts* **2017**, *7*, 59. [CrossRef]
27. Auer, F.; Blaumeiser, D.; Bauer, T.; Bösmann, A.; Szesni, N.; Libuda, J.; Wasserscheid, P. Boosting the Activity of Hydrogen Release from Liquid Organic Hydrogen Carrier Systems by Sulfur-Additives to Pt on Alumina Catalysts. *Catal. Sci. Technol.* **2019**, *9*, 3537–3547. [CrossRef]
28. Bachmann, P.; Schwarz, M.; Steinhauer, J.; Späth, F.; Düll, F.; Bauer, U.; Silva, T.N.; Mohr, S.; Hohner, C.; Scheuermeyer, M.; et al. Dehydrogenation of the Liquid Organic Hydrogen Carrier System Indole/Indoline/Octahydroindole on Pt(111). *J. Phys. Chem. C* **2018**, *122*, 4470–4479. [CrossRef]
29. Modisha, P.M.; Jordaan, J.H.L.; Bösmann, A.; Wasserscheid, P.; Bessarabov, D. Analysis of Reaction Mixtures of Perhydro-Dibenzyltoluene Using Two-Dimensional Gas Chromatography and Single Quadrupole Gas Chromatography. *Int. J. Hydrogen Energy* **2018**, *43*, 5620–5636. [CrossRef]
30. Wu, X.; Kang, F.; Duan, W.; Li, J. Density Functional Theory Calculations: A Powerful Tool to Simulate and Design High-Performance Energy Storage and Conversion Materials. *Prog. Nat. Sci. Mater. Int.* **2019**, *29*, 247–255. [CrossRef]
31. Borbáth, I.; Bakos, I.; Pászti, Z.; Szijjártó, G.P.; Tompos, A. Design of SnPt/C Cathode Electrocatalysts with Optimized Sn/Pt Surface Composition for Potential Use in Polymer Electrolyte Membrane Fuel Cells. *Catal. Today* **2021**, *366*, 20–30. [CrossRef]
32. Nagaraja, B.M.; Shin, C.H.; Jung, K.D. Selective and Stable Bimetallic PtSn/ $\theta$ -Al<sub>2</sub>O<sub>3</sub> Catalyst for Dehydrogenation of n-Butane to n-Butenes. *Appl. Catal. A Gen.* **2013**, *467*, 211–223. [CrossRef]
33. Taniya, K.; Yu, C.H.; Takado, H.; Hara, T.; Okemoto, A.; Horie, T.; Ichihashi, Y.; Tsang, S.C.; Nishiyama, S. Synthesis of Bimetallic SnPt-Nanoparticle Catalysts for Chemoselective Hydrogenation of Crotonaldehyde: Relationship between Sn<sub>x</sub>Pt<sub>y</sub> Alloy Phase and Catalytic Performance. *Catal. Today* **2018**, *303*, 241–248. [CrossRef]
34. Xu, C.; Koel, B.E. Dehydrogenation of Cyclohexene on Ordered Sn/Pt(111) Surface Alloys. *Surf. Sci.* **1994**, *304*, 249–266. [CrossRef]
35. Olivas, A.; Jerdev, D.I.; Koel, B.E. Hydrogenation of Cyclohexanone on Pt–Sn Surface Alloys. *J. Catal.* **2004**, *222*, 285–292. [CrossRef]
36. Preuster, P.; Papp, C.; Wasserscheid, P. Liquid Organic Hydrogen Carriers (LOHCs): Toward a Hydrogen-Free Hydrogen Economy. *Acc. Chem. Res.* **2017**, *50*, 74–85. [CrossRef]
37. Obodo, K.O.; Ouma, C.N.M.; Obodo, J.T.; Gebreyesus, G.; Rai, D.P.; Ukpong, A.M.; Bouhafs, B. Sn<sub>3</sub>C<sub>2</sub> Monolayer with Transition Metal Adatom for Gas Sensing: A Density Functional Theory Studies. *Nanotechnology* **2021**, *32*, 355502. [CrossRef]
38. Obodo, K.O.; Ouma, C.N.M.; Bessarabov, D. First Principles Evaluation of the OER Properties of TM–X (TM = Cr, Mn, Fe, Mo, Ru, W and Os, and X = F and S) Doped IrO<sub>2</sub> (110) Surface. *Electrochim. Acta* **2021**, *403*, 139562. [CrossRef]
39. Ouma, C.N.M.; Modisha, P.M.; Bessarabov, D. Catalytic Dehydrogenation Onset of Liquid Organic Hydrogen Carrier, Perhydro-Dibenzyltoluene: The Effect of Pd and Pt Subsurface Configurations. *Comput. Mater. Sci.* **2020**, *172*, 109332. [CrossRef]
40. Ouma, C.N.M.; Obodo, K.O.; Modisha, P.M.; Bessarabov, D. Si, P, S and Se Surface Additives as Catalytic Activity Boosters for Dehydrogenation of Methylcyclohexane to Toluene—A Liquid Organic Hydrogen Carrier System: Density Functional Theory Insights. *Mater. Chem. Phys.* **2022**, *279*, 125728. [CrossRef]
41. Wang, S.; Petzold, V.; Tripkovic, V.; Kleis, J.; Howalt, J.G.; Skulason, E.; Fernández, E.M.; Hvolbæk, B.; Jones, G.; Toftelund, A.; et al. Universal Transition State Scaling Relations for (de)Hydrogenation over Transition Metals. *Phys. Chem. Chem. Phys.* **2011**, *13*, 20760–20765. [CrossRef]

42. Yook, H.; Kim, K.; Park, J.H.; Suh, Y.W.; Han, J.W. Density Functional Theory Study on the Dehydrogenation of 1,2-Dimethyl Cyclohexane and 2-Methyl Piperidine on Pd and Pt Catalysts. *Catal. Today* **2020**, *352*, 345–353. [[CrossRef](#)]
43. Kim, K.; Oh, J.; Kim, T.W.; Park, J.H.; Han, J.W.; Suh, Y.W. Different Catalytic Behaviors of Pd and Pt Metals in Decalin Dehydrogenation to Naphthalene. *Catal. Sci. Technol.* **2017**, *7*, 3728–3735. [[CrossRef](#)]
44. Hohenberg, P.; Kohn, W. Inhomogeneous Electron Gas. *Phys. Rev.* **1964**, *136*, B864–B871. [[CrossRef](#)]
45. Kohn, W.; Sham, L.J. Self-Consistent Equations Including Exchange and Correlation Effects. *Phys. Rev.* **1965**, *140*, A1133–A1138. [[CrossRef](#)]
46. McNellis, E.R.; Meyer, J.; Reuter, K. Azobenzene at Coinage Metal Surfaces: Role of Dispersive van Der Waals Interactions. *Phys. Rev. B Condens. Matter Mater. Phys.* **2009**, *80*, 205414. [[CrossRef](#)]
47. Segall, M.D.; Lindan, J.; Probert, M.J.; Pickard, C.J.; Hasnip, P.J.; Clark, S.J.; Payne, M.C. First-Principles Simulation: Ideas, Illustrations and the CASTEP Code. *J. Phys. Condens. Matter* **2002**, *14*, 2717–2744. [[CrossRef](#)]
48. Clark, S.J.; Segall, M.D.; Pickard, C.J.; Hasnip, P.J.; Probert, M.I.J.; Refson, K.; Payne, M.C. First Principles Methods Using CASTEP. *Z. Krist.* **2005**, *220*, 567–570. [[CrossRef](#)]
49. Perdew, J.P.; Burke, K.; Ernzerhof, M. Generalized Gradient Approximation Made Simple. *Phys. Rev. Lett.* **1996**, *77*, 3865. [[CrossRef](#)] [[PubMed](#)]
50. Perdew, J.P.; Zunger, A. Self-Interaction Correction to Density-Functional Approximations for Many-Electron Systems. *Phys. Rev. B* **1981**, *23*, 5048–5049. [[CrossRef](#)]
51. Perdew, J.P.; Wang, Y. Accurate and Simple Analytic Representation of the Electron-Gas Correlation Energy. *Phys. Rev. B* **1992**, *45*, 13244–13249. [[CrossRef](#)]
52. Tkatchenko, A.; Scheffler, M. Accurate Molecular van Der Waals Interactions from Ground-State Electron Density and Free-Atom Reference Data. *Phys. Rev. Lett.* **2009**, *102*, 073005. [[CrossRef](#)] [[PubMed](#)]
53. Obodo, K.O.; Ouma, C.N.M.; Obodo, J.T.; Braun, M.; Bessarabov, D. First Principles Study of Single and Multi-Site Transition Metal Dopant Ions in MoS<sub>2</sub> Monolayer. *Comput. Condens. Matter* **2019**, *21*, e00419. [[CrossRef](#)]
54. Hamada, I. Van Der Waals Density Functional Made Accurate. *Phys. Rev. B* **2014**, *89*, 121103. [[CrossRef](#)]
55. Ouma, C.N.M.; Obodo, K.O.; Braun, M.; Amolo, G.O.; Bessarabov, D. Insights on Hydrogen Evolution Reaction in Transition Metal Doped Monolayer TcS<sub>2</sub> from Density Functional Theory Calculations. *Appl. Surf. Sci.* **2019**, *470*, 107–113. [[CrossRef](#)]